

SNX14 deficiency-induced defective axonal mitochondrial transport in Purkinje cells underlies cerebellar ataxia and can be reversed by valproate

Hongfeng Zhang^{1,†}, Yujuan Hong^{1,†}, Weijie Yang¹, Ruimin Wang¹, Ting Yao¹, Jian Wang¹, Ke Liu², Huilong Yuan¹, Chaoqun Xu², Yuanyuan Zhou¹, Guanxian Li¹, Lishan Zhang¹, Hong Luo¹, Xian Zhang¹, Dan Du³, Hao Sun¹, Qiuyang Zheng¹, Yun-Wu Zhang¹, Yingjun Zhao¹, Ying Zhou², Huaxi Xu¹ and Xin Wang^{1,*}

¹State Key Laboratory of Cellular Stress Biology, Fujian Provincial Key Laboratory of Neurodegenerative Disease and Aging Research, Institute of Neuroscience, School of Medicine, Xiamen University, Xiamen, Fujian, 361102, China

²National Institute for Data Science in Health and Medicine, School of Medicine, Xiamen University, Xiamen, Fujian, 361102, China

³Cancer Research Center, Department of Stomatology, School of medicine, Xiamen University, Xiamen, Fujian, 361102, China

† These authors contributed equally to this work

*Correspondence: wangx@xmu.edu.cn

Abstract

Loss-of-function mutations in *SNX14* cause autosomal recessive spinocerebellar ataxia 20, which is a form of early-onset cerebellar ataxia that lacks molecular mechanisms and mouse models. We generated *Snx14*-deficient mouse models and observed severe motor deficits and cell-autonomous Purkinje cell degeneration. *SNX14* deficiency disrupted microtubule organization and mitochondrial transport in axons by destabilizing the microtubule-severing enzyme spastin, which is implicated in dominant hereditary spastic paraplegia with cerebellar ataxia, and compromised axonal integrity and mitochondrial function. Axonal transport disruption and mitochondrial dysfunction further led to degeneration of high-energy-demanding Purkinje cells, which resulted in the pathogenesis of cerebellar ataxia. The antiepileptic drug valproate ameliorated motor deficits and cerebellar degeneration in *Snx14*-deficient mice via the restoration of mitochondrial transport and function in Purkinje cells. Our study revealed an unprecedented role for *SNX14*-dependent axonal transport in cerebellar ataxia, demonstrated the convergence of *SNX14* and spastin in mitochondrial dysfunction, and suggests valproate as a potential therapeutic agent.

Keywords: sorting nexin 14, cerebellar ataxia, Purkinje cell degeneration, mitochondrial dysfunction, axonal transport, valproate.

Introduction

Ataxia is a debilitating nervous system disorder that manifests as impaired autonomous coordination of limb movements. Etiologically, ataxia is a complex disease that is induced by a combination of environmental and genetic factors [1]. Cumulative evidence indicates that genetic factors play key roles in ataxia [2]. Hereditary ataxia is classified into autosomal dominant, autosomal recessive and X-linked forms. The incidence of autosomal recessive cerebellar ataxia (ARCA) is approximately 3 cases per 100,000 individuals, with overlapping symptoms, such as cerebellar atrophy or hypoplasia [3]. Cerebellar Purkinje cell dysfunction or degeneration is a primary pathological event in patients and animal models with cerebellar ataxia [4-6]. Clinically, patients with ARCA exhibit gait irregularities, imbalance, difficulties with swallowing, dyskinesia and other features related to motor function. Despite the severity of impairment associated with ARCA, its mechanisms remain elusive, and no specific treatments have been described.

Recent studies [7, 8] reported the identification of a new type of early-onset ARCA, autosomal recessive spinocerebellar ataxia 20 (SCAR20). SCAR20 patients exhibit early-onset cerebellar atrophy, severe motor ataxia, moderate to severe mental retardation, and autistic behavior. Whole-exome sequencing analysis identified the sorting nexin 14 (*SNX14*) gene as a candidate gene locus for SCAR20 onset, and *SNX14* loss-of-function mutations account for approximately 9.9% of early-onset cerebellar atrophy and ataxia cases, which represents a higher percentage than any other potential genes related to cerebellar atrophy, such as *GRID2* (2.47%), *NPC1* (1.23%), and *SETX* (1.23%) [7]. *SNX14* is a member of the

sorting nexin (SNX) family, which consists of 33 related proteins comprised of a conserved phosphoinositol-binding phospho homology (PX) domain that facilitates the regulation of vesicular transport and protein sorting [9]. Our work and other studies demonstrated that SNXs play important roles in multiple neurodegenerative diseases [10-14]. Recent studies also indicated that SNX14 regulated lipid metabolism in fibroblasts from individuals with *SNX14* mutations and in *SNX14*-depleted cell lines [15]. Although SNX14 is highly expressed in the central nervous system [16-18], the pathophysiological functions of SNX14 in SCAR20 onset are largely unknown, and therapeutic strategies for SCAR20 have not been elucidated.

The present study showed that *Snx14*-deficient mouse models recapitulated the pathological manifestations of SCAR20 patients, in which Nestin-Cre-mediated SNX14 deletion in neurons and glia induced defects in axonal transport, mitochondrial dysfunction, and progressive loss of Purkinje cells. Purkinje cell degeneration aggravated cerebellar degeneration via enhanced microglial activation and inflammatory cytokine production. Notably, valproate (VPA) treatment in *Snx14*-deficient mice reversed impairments in motor coordination, Purkinje cell death, and mitochondrial dysfunction. Together, we established mouse models that reproduced SCAR20 pathology, described the associated mechanisms underlying SCAR20 pathogenesis, and identified the use of the antiepileptic agent VPA as a potential corrective therapy for cerebellar atrophy and ataxia.

Results

SNX14 deficiency causes progressive cerebellar ataxia and atrophy

Snx14^{flox/flox} (*Snx14^{ff}*) mice were generated via the targeted deletion of exons 9-12 of the murine *Snx14* gene, where most homologous human mutations in SCAR20 were previously identified (Figure S1A). Constitutive *Snx14* deletion produced no viable *Snx14^{-/-}* offspring in multiple crosses between heterozygous breeding pairs (*Snx14^{+/-}* × *Snx14^{+/-}*) (Figure S1B). Embryonic lethality was confirmed in pups prior to birth at embryonic day 12.5 (E12.5) (Figure S1C). Therefore, we generated a conditional *Snx14*-knockout mouse model in neurons and glia by crossing *Snx14^{ff}* mice with a *Nestin-Cre* line. *Snx14^{ff};Nestin-Cre* (cKO) mice showed normal viability and fertility, and we confirmed that SNX14 expression was ablated in the central nervous system and retained in other tissues (Figure S1D-S1F).

Snx14 cKO mice had similar lifespan (Figure S1G) and body weight (Figure S1H) as *Snx14^{+/+}; Nestin-Cre* mice (cHet). To evaluate the effects of *Snx14* deletion in the CNS on motor coordination, we compared rotarod and balance beam performance in cKO and wild-type (WT) animals. We found that cKO mice showed mild impairment in motor coordination from 1 month of age, which progressively deteriorated in animals at 2 and 3 months according to rotarod tests (Figure 1A and S1I). Similar deficits in motor coordination were observed in male and female cKO mice in the balance beam tests (Figure 1B, 1C, S1J, S1K and Movie S1).

We also examined morphological changes in the brain and observed that the cerebella of 3-month-old cKO mice were smaller in size and weight than those of

control mice (Figure S2A). Further histological analyses revealed a reduction in the thickness of the cerebellar molecular layer (ML), which is a region enriched with Purkinje cell dendrites (Figure S2B), but no obvious differences were observed in the thickness of the granular layer (GL) (Figure S2C), the thickness of the cerebral cortex or the number of NeuN⁺ neurons in the cerebral cortex (Figure S2D and S2E), which suggests that Purkinje cells within the cerebellum are specifically susceptible to SNX14 deletion. These results demonstrate that SNX14 deficiency induces progressive ataxia phenotypes and cerebellar atrophy.

SNX14 deficiency induces progressive cerebellar Purkinje cell degeneration and microglial activation

Although no changes in Purkinje cell pathology were observed in 1-month-old cKO mice, ~30% and ~40% reductions in Purkinje cells were observed in 2- and 3-month-old cKO mice, respectively, compared to cHet mice (Figure 1D and 1E). We examined whether SNX14 haploinsufficiency affected Purkinje cell survival using immunohistochemical analysis and found a normal density of Purkinje cells in cHet mice compared to littermate *Snx14^{fl/fl}* (WT) mice (Figure S2F). Notably, enhanced neuropathological effects were observed in female cKO mice compared to males (Figure S2G). No change in cerebellar granule cell number was observed at the age of 3 months, as quantified by NeuN levels (Figure S2H). We observed that the Purkinje cell number negatively correlated with foot slips in balance beam tests (Figure 1F), which suggests SNX14-dependent Purkinje cell degeneration in motor

impairment.

To further characterize SNX14-dependent morphological alterations in Purkinje cells, we performed immunofluorescence staining using the Purkinje cell marker carbonic anhydrase 8 (CA8) and observed swollen axons in ~16% CA8-positive Purkinje cells in 2-month-old cKO mice (Figure 1G and 1H). We also observed aberrant accumulation of mitochondria, lysosomes and other organelles in swollen axons using transmission electron microscopy (TEM) (Figure 1I, S3A and S3B). In addition to axonal swelling, other axonopathological features (Figure 1I and 1J) and hypomyelination (Figure S3C-S3E) were observed in cKO mice. Axonal swelling was evident in cKO mice from 1 month of age (Figure S3F and S3G), which suggests that axonopathy in Purkinje cells is an early event in SCAR20 pathogenesis and onset.

To determine whether Purkinje cell degeneration induced neuroinflammation, we performed double immunostaining using ionized calcium binding adaptor molecule 1 (IBA1) and CA8 antibodies. We observed significant microglial proliferation and activation associated with Purkinje cell degeneration in the cerebella of 2-month-old but not 1-month-old cKO mice (Figure S4A-S4D). Purkinje cell number and microglial abundance were inversely correlated (Figure S4E). We subsequently observed an upregulation of the mRNA expression of proinflammatory cytokines, such as tumor necrosis factor (*Tnf*) and interleukin 1 β (*Ilb*), in *Snx14*-deficient mouse cerebella using quantitative reverse transcription polymerase chain reaction (qRT-PCR) analysis (Figure S4F).

SNX14 deficiency induces cell-autonomous death in Purkinje cells

Snx14 mRNA is predominately expressed in the Purkinje cells of the mouse cerebellum (Figure S5). Therefore, we hypothesized that SNX14 was essential for Purkinje cell survival. To test this hypothesis, we generated a cell-specific *Snx14* KO mouse model in Purkinje cells by crossing *Snx14^{fl/fl}* with a *Pcp2-Cre* transgenic mouse line. We first evaluated motor coordination using balance beam tests. Little or no impairment in motor coordination was observed in 1- and 2-month-old male *Snx14^{fl/fl};Pcp2-Cre* animals, but the 3- and 4-month-old *Snx14^{fl/fl};Pcp2-Cre* mice required a longer time to cross the balance beam and exhibited more foot slips than control mice (Figure 2A). Notably, impaired motor coordination was enhanced in female *Snx14^{fl/fl};Pcp2-Cre* mice compared to male mice (Figure S6A and S6B).

Similar to the cKO mice, male and female *Snx14^{fl/fl};Pcp2-Cre* mice exhibited a progressive loss of Purkinje cells with age (Figure 2B and S6C). More than 20% of Purkinje cells in 3-month-old *Snx14^{fl/fl};Pcp2-Cre* mice exhibited swollen axons (Figure 2C and 2D). Similar to cKO mice, ultrastructural analysis revealed significant axonopathy in *Snx14^{fl/fl};Pcp2-Cre* mice (Figure 2E and 2F) and glial activation in 3- and 4-month-old *Snx14^{fl/fl};Pcp2-Cre* mice (Figure S6D-S6K). These results indicate that cell-autonomous Purkinje cell death and axon degeneration are pathological features of SCAR20.

To determine whether hypomyelination contributed to the neuropathological features observed in cKO mice, we selectively deleted *Snx14* in oligodendrocyte lineage cells by breeding *Snx14^{fl/fl}* mice with *Olig1-Cre* transgenic mice. Although

cerebellar hypomyelination was evident in transgenic *Snx14^{fl/fl};Olig1-Cre* mice (Figure S7A-S7C), no alterations in motor coordination (Figure S7D and S7E) and only a slight reduction (~15% loss) in Purkinje cells (Figure S7F-S7H) were observed in these animals up to 6 months of age. Taken together, these results indicate that Purkinje cell degeneration likely drives SCAR20 pathogenesis, with little or no contribution from oligodendrocyte dysfunction.

Mitochondrial dysfunction in *Snx14*-deficient Purkinje cells

To determine the underlying molecular mechanism of Purkinje cell degeneration in SCAR20, we characterized global proteomic expression profiles in 1-month-old (the early phase of disease progression) cHet and cKO mouse cerebella using tandem mass tag (TMT)-based quantitative proteomics. A total of 222 significantly upregulated and 352 downregulated differentially expressed proteins (DEPs) were identified (Figure 3A). We confirmed the expression of several downregulated proteins from the proteomic study using immunoblot analysis, such as CHCHD4 (mitochondria-related), SNX1 (protein sorting-related), MBP and MOG (myelin-related). As expected, the expression levels of these proteins were markedly reduced in the cerebellum of cKO mice compared to cHet mice (Figure S8).

Notably, we observed an enrichment of mitochondrial components in downregulated DEPs (Figure 3B). Gene Ontology (GO) analysis of relevant biological process (BP) pathways revealed a downregulation of proteins related to mitochondrial respiratory chain complex biogenesis/assembly and the cellular response to reactive

oxygen species (ROS) (Figure 3C). These results suggest a role for SNX14 in homeostatic mitochondrial function. Therefore, we examined whether SNX14 deficiency altered mitochondrial function in the mouse cerebellum. As expected, ATP production was markedly reduced in the cerebellum of cKO mice (Figure 3D). We also observed a marked reduction in CI- and CII-linked oxidative phosphorylation (OXPHOS) (CI_P and CI&II_P) using high-resolution FluoRespirometry and a reduced maximal capacity of the mitochondrial electron transport system (ETS) (CI&II_E) in cKO compared to cHet mouse cerebella (Figure 3E). These results indicate that *Snx14* deficiency impairs mitochondrial respiration in the cerebellum.

Dysfunction of the mitochondrial respiratory chain generally leads to the overproduction of mitochondrial reactive oxygen species (ROS), which induces cellular damage [19]. To determine whether SNX14 deletion affected ROS production in Purkinje cells, we crossed *Snx14^{ff};Pcp2-Cre* mice with a red fluorescent protein reporter (R26-LSL-tdTomato) mouse line to obtain *Snx14^{ff};Pcp2-Cre;tdTomato* (KO) and *Snx14^{ff/+};Pcp2-Cre;tdTomato* (Het) mice to induce exclusive tdTomato expression in cerebellar Purkinje cells (Figure S9A). The tdTomato-expressing Purkinje cells in newborn mice (P6) were isolated using flow cytometry sorting (FACS) and cultured *in vitro* for 5 days (Figure 3F). We used the fluorescent probe 2',7'-dichlorofluorescein-diacetate (DCFH-DA) to quantify ROS production and observed increased ROS production in *Snx14* KO cells compared to *Snx14* Het Purkinje cells (Figure 3G and 3H). *Snx14* KO Purkinje cells exhibited reduced cellular sizes (Figure S9B) and branch complexity (Figure S9C and S9D). Together, these

results indicate that *Snx14* deficiency impairs cerebellar mitochondrial function in Purkinje cells.

SNX14 deficiency impairs mitochondrial transport in axons and destabilizes spastin

We observed an accumulation of smaller mitochondria (Figure 4A and 4B) and marked microtubule disorganization (Figure 4A and 4C) in the swollen axons from *Snx14*-deficient Purkinje cells. Because axonal cargo transport is dependent on linear microtubule organization, we hypothesized that SNX14 deficiency would disrupt the microtubule-based transport of organelles, such as mitochondria. Microtubule misalignment and disorganization ultimately induce altered mitochondrial distribution along the axon and cause mitochondrial dysfunction. Therefore, we monitored mitochondrial motility in the axons of *Snx14*-deficient neurons using real-time microscopic imaging. As expected, markedly fewer motile mitochondria were observed in the axons of *Snx14* KO neurons than in Het neurons (Figure 4D and Movie S2). Anterograde and retrograde mitochondrial transport was compromised. However, SNX14 deficiency appeared to affect anterograde transport to a greater extent (Figure 4D).

As a member of the SNX family, SNX14 likely functions as an intracellular trafficking regulator via interactions with other proteins. To identify SNX14-binding proteins, HEK293T cells were transfected with a hemagglutinin (HA)-tagged SNX14 (SNX14-HA) plasmid and then subjected to immunoprecipitation (IP) using an anti-HA

antibody. We identified multiple potential SNX14-interacting proteins using proteomic analysis (Figure 4E, 4F and Table S2), including the microtubule-severing protein spastin, which is required to maintain axonal integrity [20]. Similar to *SNX14*, *SPAST* (the spastin coding gene) haploinsufficiency also induces axonal swelling and impairs mitochondrial transport [21, 22]. We confirmed the interactions between spastin and SNX14 using co-IP (Figure 4G) and *in vitro* pulldown assays (Figure S10A) and demonstrated that spastin and SNX14 formed a complex. Moreover, we observed colocalization of SNX14 and spastin and that SNX14-spastin puncta partially colocalized with the lipid droplet marker BODIPY in HeLa cells (Figure S10B). To determine the critical interaction domains of each protein, we performed domain mapping assays using truncated spastin and SNX14 protein fragments. We found that deletion of the N-terminal domain (1-86 aa, M87 form) of spastin completely abolished the interaction between spastin and SNX14, and deletion of the hydrophobic region (HR) (49-80 aa, ΔHR) largely disrupted the interaction (Figure S10B). However, the microtubule interacting and endosomal trafficking (MIT) domain and the microtubule-binding (MBD) and AAA ATPase (AAA) domains of spastin were not essential for the spastin-SNX14 interaction (Figure S10C). Moreover, we found that the PXA, RGS, PX, and PXC domains of the SNX14 protein were not required for the SNX14-spastin interaction (Figure S10D); however, a SNX14 N-terminal fragment with transmembrane domains (SNX14-TM, aa 1-130) can interact with M1 spastin (Figure S10E). Together, these results indicated that the N-terminal fragment of M1 spastin (aa1-86) and the N-terminal fragment of SNX14 (aa1-130) are required for

their interaction.

Spastin protein levels were downregulated in the cerebella of cKO mice compared to cHet mice (Figure 4H), but *SPAST* mRNA levels were not changed (Figure 4I), which suggests that SNX14 regulates spastin expression posttranscriptionally. We observed that enhanced spastin turnover with SNX14 deficiency was largely reversed by the inhibition of lysosomal, rather than proteasomal, protein degradation (Figure 4J). To determine whether the restoration of spastin protein expression rescued defective mitochondrial transport in the axons of *Snx14* KO neurons, we infected *Snx14* KO neurons with recombinant SPAST adeno-associated virus (rAAV) and observed that M1 spastin overexpression largely restored mitochondrial motility in *Snx14* KO neurons (Figure S11). These results indicate that SNX14 deficiency-induced spastin degradation accounts for defective mitochondrial transport in axons.

VPA treatment ameliorates the pathological effects associated with SNX14 deficiency

VPA is an antiepileptic drug that is also used to treat bipolar disorder. VPA enhanced mitochondrial function in SH-SY5Y cells [23] and axonal remodeling in cultured neurons [24]. Therefore, we determined whether VPA reversed mitochondrial dysfunction and Purkinje cell degeneration in *Snx14* KO mice. Postnatal day 25 (P25) cKO mice were given a daily intraperitoneal dose of VPA (250 mg/kg) or saline for 35 consecutive days and subsequently assayed for behavior and cerebellar physiology

(Figure 5A). The administration of VPA at subchronic levels did not produce any apparent toxic effects, such as weight gain, which was similar between the cKO + VPA and cKO + saline groups (Figure S12A). Notably, subchronic injections of VPA markedly improved motor coordination in male and female cKO mice in the balance beam tests (Figure 5B, S12B and Movie S3). In the cKO mouse cerebellum, VPA treatment restored the thickness of the ML (Figure 5C and 5D) and reduced the loss of Purkinje cells (Figure 5C, 5E and S12C). VPA treatment similarly reversed Purkinje cell degeneration in *Snx14^{fl/fl}; Pcp2-Cre* mice (Figure S12D-S12F). Transcriptomic analysis revealed that 781 genes were downregulated in the cerebellum of cKO mice compared to cHet animals, and 64 of these genes were partially restored with VPA treatment (Figure 5F). Notably, most of the restored gene signatures were Purkinje cell-specific (49 of 64) (Figure 5G and S12G). The expression profiles of the cKO cerebellum showed robust changes in neuroinflammatory signatures (Figure S12H), and VPA administration normalized the expression of microglia- and astrocyte-specific genes (Figure S12I and S12J). Consistent with the transcriptomic analysis, VPA treatment attenuated microglial proliferation and activation in the cKO cerebellum (Figure S12K-S12M). To determine whether VPA specifically conferred neuroprotective effects to Purkinje cells, we treated Purkinje cells with VPA *in vitro* and evaluated the consequent effects on morphology. We found that VPA treatment restored cellular size and branch complexity in *Snx14* KO Purkinje cells (Figure 5H and 5I).

Although the pharmacological effects of VPA as an antiepileptic agent are not

clear, VPA has broad inhibitory activity toward class I and II histone deacetylases (HDACs) [25]. HDAC inhibitors reversed cytotoxicity in cellular and fly models of Parkinson's disease [26]. Therefore, VPA may confer neuroprotective effects via HDAC inhibition. To test this hypothesis, we evaluated the effects of two widely used HDAC inhibitors, SAHA and panobinostat, on the restoration of SNX14 deficiency-induced motor impairment and found that neither compound ameliorated the motor coordination deficits and Purkinje cell loss in cKO mice (Figure S13A-S13F). These results suggest that VPA exerts its rescuing effects in an HDAC-independent manner.

A possible link between SNX14 and lipid metabolism was proposed [15, 27-30]. Lipid metabolism malfunction is a major feature of Niemann Pick Disease Type C (NPC) [31], and patients with NPC also exhibit progressive cerebellar degeneration that is similar to SCAR20 [32, 33]. Therefore, we examined whether the therapeutic strategy for NPC was beneficial for SCAR20. However, the widely used cholesterol chelator HP- β -CD, which was effective in cell and mouse models of NPC [34, 35], failed to ameliorate cerebellar degeneration and motor deficits in *Snx14*-deficient mice (Figure S13G-S13I), which suggests that *SNX14* deletion induces SCAR20 by signaling pathways other than regulation of the accumulation of unesterified cholesterol.

VPA promotes Purkinje cell survival via restoration of mitochondrial function

To examine the mechanisms underlying the therapeutic effects of VPA treatment, we

characterized neuronal physiology in *Snx14* KO animals treated with VPA. VPA administration markedly mitigated axonopathies and microtubule disorganization (Figure 6A-6C). VPA treatment also relieved the abnormal axonal accumulation of mitochondria in *Snx14*-deficient Purkinje cells (Figure 6D). At the molecular level, VPA treatment restored the protein levels of spastin (Figure S14A) and polymerized α -tubulin (Figure S14B) in *Snx14* KO neurons. Axonal transport deficits may lead to mitochondrial accumulation. Therefore, we characterized axonal mitochondrial motility using time-lapse microscopy. We found that VPA treatment markedly restored mitochondrial motility in *Snx14* KO neuronal axons (Figure 6E). We investigated the effects of VPA on cerebellar mitochondrial function and observed significant increases in cerebellar mitochondrial respiratory capacity with VPA treatment, including the respiration levels of CI- and CII-linked OXPHOS and the maximal capacity of the mitochondrial ETS (Figure 6F). We also observed that VPA treatment decreased ROS production in KO Purkinje cells compared to saline controls (Figure 6G). Taken together, these results suggest that VPA treatment promotes Purkinje cell survival by reversing mitochondrial dysfunction in *Snx14*-deficient mice.

Discussion

SNX14 loss-of-function mutations were identified in patients with cerebellar atrophy, intellectual disabilities and autism [7, 8], which suggests a critical role of *SNX14* in brain function. Deletion of *Snx14* in neurons and glia recapitulated human SCAR20 neurological phenotypes, including the impaired coordination of limb movements and Purkinje cell loss previously reported in SCAR20 patients. These results demonstrated that *SNX14* dysfunction was sufficient to drive pathological phenotypes with full penetrance and provide a robust model system to characterize SCAR20-associated degeneration.

Multiple cerebellar cell types contribute to the pathogenesis of cerebellar ataxia [36, 37]. To identify the most vulnerable cell types in SCAR20, we generated Purkinje cell-specific (*Snx14^{ff};Pcp2-Cre*) and oligodendrocyte lineage cell-specific (*Snx14^{ff};Olig1-Cre*) *Snx14* KO mice. Notably, *Snx14^{ff};Pcp2-Cre* mice recapitulated most of the behavioral and morphological phenotypes of cKO mice. However, *Snx14^{ff};Olig1-Cre* mice exhibited only hypomyelination without behavioral deficits. Therefore, Purkinje cell degeneration triggers SCAR20 pathogenesis in a cell-autonomous manner. Contributions from other cell types cannot be completely discounted because phenotypes in *Snx14^{ff};Pcp2-Cre* mice were slightly delayed by ~2 weeks compared to *Snx14^{ff};Nestin-Cre* mice. Therefore, the contributions of other cell types in cerebellar ataxia require further investigation.

SNX family proteins play essential roles in intracellular cargo transport, and these proteins are linked to a number of neurodegenerative diseases [38]. Our study

revealed that SNX14 was the first SNX protein to regulate mitochondrial transport and function via the modulation of microtubule organization. We found interactions between SNX14 and the microtubule-severing enzyme spastin, SNX14 deficiency disrupted microtubule organization, and reduced spastin expression. Moreover, SPAST haploinsufficiency in human and animal models causes hereditary spastic paraplegia with cerebellar ataxia via disrupting microtubule organization and axonal transport of cargoes (including mitochondria) [39, 40]. These results demonstrated the convergence of SCAR20 and HSP on a SNX14/spastin pathway (Figure S15). Future investigations will determine whether SNX14 also regulates its microtubule-severing activity.

Mitochondrial dysfunction is a common pathological feature of neurodegenerative diseases, such as Huntington's disease [41], Parkinson's disease [42], Alzheimer's disease [43], amyotrophic lateral sclerosis [44] and certain types of cerebellar ataxias (SCA1 [45-47] and Friedreich's ataxia [48]). The present study discovered an unidentified convergence of SNX14 and spastin in mitochondrial transport and dysfunction and demonstrated the possibility of the restoration of mitochondrial function by targeting of the pathway in the treatment of cerebellar degeneration.

SNX14 mutations led to increased levels of fatty acids in model animals [28, 29] and cholesterol accumulation in human fibroblasts [15]. Moreover, M1 spastin requires its lipid droplet binding N-terminal HR domain to interact with SNX14, suggesting that lipid droplets may provide a niche for the interaction between SNX14 and spastin. SNX14 and spastin could work together at lipid droplets and play a role in fatty acid

and lipid metabolism. As mitochondria play a major role in fatty acid oxidation and mitochondrial defects lead to lipid droplet accumulation [49], SNX14 deficiency-mediated mitochondrial dysfunction could also disrupt fatty acid oxidation and lipid droplet accumulation. Our study revealed that HP- β -CD, a potential therapy for NPC [34, 35], failed to ameliorate cerebellar degeneration in *Snx14*-deficient mice, which suggests that SNX14 deletion may lead to Purkinje cell degeneration through a cholesterol-independent mechanism. Future investigations are required to determine whether SNX14 regulates the metabolism of neutral lipids other than cholesterol.

VPA is traditionally used as an antiepileptic agent [50], and it was originally discovered to affect GABA levels, block voltage-gated sodium channels, and inhibit HDAC activity [51]. Our study found that VPA promoted Purkinje cell survival by restoring microtubule organization and mitochondrial function (Figure S15). Purkinje cell degeneration and neuroinflammation are typical symptoms of cerebellar ataxia, and VPA improved symptoms that corresponded to the major domains of ataxia, including motor function, Purkinje cell degeneration and neuroinflammation, in our murine model. Therefore, our data suggest that VPA would be an effective treatment for SCAR20 and other types of cerebellar ataxia. However, the therapeutic potential of VPA for the treatment of cerebellar ataxia warrants rigorous evaluation in future clinical studies in SCAR20 patients.

In summary, our elucidation of SNX14 in the regulation of mitochondrial transport in axons provides new mechanistic insights into the pathogenesis of cerebellar ataxia.

Notably, we propose the chronic administration of the antiepileptic drug VPA as a potential treatment for patients with SNX14 deficiency.

Methods

The detailed methods and materials are available as Supplementary data.

Author contributions

X.W. and H.Z. conceived and designed the study. X.W., H.Z. and Y.H. analyzed the data and wrote the manuscript. H.Z., Y.H., W.Y., R.W., T.Y., J.W. and Yuanyuan.Zhou. performed the behavioral and morphological analyses. H.Z., Y.H., R.W., G.L., Q.Z. L.Z., H.L., X.Z. and H.S. performed the biochemical experiments. H.Z. and Y.H. performed mitochondrial function analyses. K.L., C.X. and Ying.Zhou. performed the bioinformatics analyses. H.Y. and Yingjun.Zhao. performed AAV production. D.D. provided technical assistance in lentiviral production. H.X. and Y.W.Z. discussed and edited the manuscript. All authors read and approved the manuscript.

Acknowledgments

We thank Tim Huang for helpful discussion, Wei Mo for sharing mouse lines, Li Zhong for sharing reagents, Aidong Han, Luming Yao, Caiming Wu, Mingxia Zhu, Qingfeng Liu, Lin Zhu, Shuo Zhang, Haiping Zheng, and Changchuan Xie for technical assistance, and Cui Li for providing bioinformatics software. We also thank Novogene Co., Ltd. and PTM Biolab Co., Ltd. for technical assistance in the transcriptomic and proteomic analyses, respectively.

Funding

This work was supported in part by the National Natural Science Foundation of China (81822014, 31871077 and 81571176 to X.W., 81701349 to H.Z., 81802823 to Y.Z.), National Key R&D Program of China (2016YFC1305900 to X.W.), Natural Science Foundation of Fujian Province of China (2017J06021 to X.W., 2018J01054 to Y.Z.), and the Fundamental Research Funds for the Chinese Central Universities (20720150061 to X.W.).

Conflict of Interest

None declared.

References

1. Akbar U, Ashizawa T Ataxia. *Neurol Clin* 2015;**33**(1):225-48. doi: 10.1016/j.ncl.2014.09.004.
2. Anheim M, Tranchant C, Koenig M The autosomal recessive cerebellar ataxias. *N Engl J Med* 2012;**366**(7):636-46. doi: 10.1056/NEJMra1006610.
3. Ruano L, Melo C, Silva MC, et al. The global epidemiology of hereditary ataxia and spastic paraplegia: a systematic review of prevalence studies. *Neuroepidemiology* 2014;**42**(3):174-83. doi: 10.1159/000358801.
4. Zhou L, Yang D, Wang DJ, et al. Numb deficiency in cerebellar Purkinje cells impairs synaptic expression of metabotropic glutamate receptor and motor coordination. *Proc Natl Acad Sci U S A* 2015;**112**(50):15474-9. doi: 10.1073/pnas.1512915112.

5. Zhou JH, Wang XT, Zhou L, et al. Ablation of TFR1 in Purkinje Cells Inhibits mGlu1 Trafficking and Impairs Motor Coordination, But Not Autistic-Like Behaviors. *J Neurosci* 2017;**37**(47):11335-11352. doi: 10.1523/JNEUROSCI.1223-17.2017.
6. Liu C, Mei M, Li Q, et al. Loss of the golgin GM130 causes Golgi disruption, Purkinje neuron loss, and ataxia in mice. *Proc Natl Acad Sci U S A* 2017;**114**(2):346-351. doi: 10.1073/pnas.1608576114.
7. Akizu N, Cantagrel V, Zaki MS, et al. Biallelic mutations in SNX14 cause a syndromic form of cerebellar atrophy and lysosome-autophagosome dysfunction. *Nat Genet* 2015;**47**(5):528-34. doi: 10.1038/ng.3256.
8. Thomas AC, Williams H, Seto-Salvia N, et al. Mutations in SNX14 cause a distinctive autosomal-recessive cerebellar ataxia and intellectual disability syndrome. *Am J Hum Genet* 2014;**95**(5):611-21. doi: 10.1016/j.ajhg.2014.10.007.
9. Worby CA, Dixon JE Sorting out the cellular functions of sorting nexins. *Nat Rev Mol Cell Biol* 2002;**3**(12):919-31. doi: 10.1038/nrm974.
10. Zhao Y, Wang Y, Yang J, et al. Sorting nexin 12 interacts with BACE1 and regulates BACE1-mediated APP processing. *Mol Neurodegener* 2012;**7**:30. doi: 10.1186/1750-1326-7-30.
11. Wang X, Zhao Y, Zhang X, et al. Loss of sorting nexin 27 contributes to excitatory synaptic dysfunction by modulating glutamate receptor recycling in Down's syndrome. *Nat Med* 2013;**19**(4):473-80. doi: 10.1038/nm.3117.
12. Wang X, Huang T, Zhao Y, et al. Sorting nexin 27 regulates Abeta production through modulating gamma-secretase activity. *Cell Rep* 2014;**9**(3):1023-33. doi:

10.1016/j.celrep.2014.09.037.

13. Huang TY, Zhao Y, Li X, et al. SNX27 and SORLA Interact to Reduce Amyloidogenic Subcellular Distribution and Processing of Amyloid Precursor Protein. *J Neurosci* 2016;**36**(30):7996-8011. doi: 10.1523/JNEUROSCI.0206-16.2016.

14. Loo LS, Tang N, Al-Haddawi M, et al. A role for sorting nexin 27 in AMPA receptor trafficking. *Nat Commun* 2014;**5**:3176. doi: 10.1038/ncomms4176.

15. Bryant D, Liu Y, Datta S, et al. SNX14 mutations affect endoplasmic reticulum-associated neutral lipid metabolism in autosomal recessive spinocerebellar ataxia 20. *Hum Mol Genet* 2018;**27**(11):1927-1940. doi: 10.1093/hmg/ddy101.

16. Carroll P, Renoncourt Y, Gayet O, et al. Sorting nexin-14, a gene expressed in motoneurons trapped by an in vitro preselection method. *Dev Dyn* 2001;**221**(4):431-42. doi: 10.1002/dvdy.1163.

17. Huang HS, Yoon BJ, Brooks S, et al. Snx14 regulates neuronal excitability, promotes synaptic transmission, and is imprinted in the brain of mice. *PLoS One* 2014;**9**(5):e98383. doi: 10.1371/journal.pone.0098383.

18. Ha CM, Park D, Kim Y, et al. SNX14 is a bifunctional negative regulator for neuronal 5-HT6 receptor signaling. *J Cell Sci* 2015;**128**(9):1848-61. doi: 10.1242/jcs.169581.

19. Zorov DB, Juhaszova M, Sollott SJ Mitochondrial reactive oxygen species (ROS) and ROS-induced ROS release. *Physiol Rev* 2014;**94**(3):909-50. doi: 10.1152/physrev.00026.2013.

20. Roll-Mecak A, Vale RD Structural basis of microtubule severing by the hereditary spastic paraplegia protein spastin. *Nature* 2008;**451**(7176):363-U16. doi: 10.1038/nature06482.

21. Tarrade A, Fassier C, Charvin D, et al. A mutation of spastin is responsible for swellings and impairment of transport in a region of axon characterized by changes in microtubule composition. *Human Molecular Genetics* 2006;**15**(24):3544-3558. doi: 10.1093/hmg/ddl431.
22. Denton KR, Lei L, Grenier J, et al. Loss of spastin function results in disease-specific axonal defects in human pluripotent stem cell-based models of hereditary spastic paraplegia. *Stem Cells* 2014;**32**(2):414-23. doi: 10.1002/stem.1569.
23. Bachmann RF, Wang Y, Yuan PX, et al. Common effects of lithium and valproate on mitochondrial functions: protection against methamphetamine-induced mitochondrial damage. *International Journal of Neuropsychopharmacology* 2009;**12**(6):805-822. doi: 10.1017/S1461145708009802.
24. Biermann J, Grieshaber P, Goebel U, et al. Valproic acid-mediated neuroprotection and regeneration in injured retinal ganglion cells. *Invest Ophthalmol Vis Sci* 2010;**51**(1):526-34. doi: 10.1167/iops.09-3903.
25. Gottlicher M, Minucci S, Zhu P, et al. Valproic acid defines a novel class of HDAC inhibitors inducing differentiation of transformed cells. *EMBO J* 2001;**20**(24):6969-78. doi: 10.1093/emboj/20.24.6969.
26. Kontopoulos E, Parvin JD, Feany MB Alpha-synuclein acts in the nucleus to inhibit histone acetylation and promote neurotoxicity. *Hum Mol Genet* 2006;**15**(20):3012-23. doi: 10.1093/hmg/ddl243.
27. Datta S, Bowerman J, Hariri H, et al. Snx14 proximity labeling reveals a role in saturated fatty acid metabolism and ER homeostasis defective in SCAR20 disease. *Proc Natl Acad Sci U S A* 2020. doi: 10.1073/pnas.2011124117.

28. Ugrankar R, Bowerman J, Hariri H, et al. Drosophila Snazarus Regulates a Lipid Droplet Population at Plasma Membrane-Droplet Contacts in Adipocytes. *Dev Cell* 2019;**50**(5):557-572 e5. doi: 10.1016/j.devcel.2019.07.021.
29. Bryant D, Seda M, Peskett E, et al. Diverse species-specific phenotypic consequences of loss of function sorting nexin 14 mutations. *Sci Rep* 2020;**10**(1):13763. doi: 10.1038/s41598-020-70797-2.
30. Datta S, Liu Y, Hariri H, et al. Cerebellar ataxia disease-associated Snx14 promotes lipid droplet growth at ER-droplet contacts. *J Cell Biol* 2019;**218**(4):1335-1351. doi: 10.1083/jcb.201808133.
31. Liscum L, Ruggiero RM, Faust JR The intracellular transport of low density lipoprotein-derived cholesterol is defective in Niemann-Pick type C fibroblasts. *J Cell Biol* 1989;**108**(5):1625-36. doi: 10.1083/jcb.108.5.1625.
32. Elrick MJ, Pacheco CD, Yu T, et al. Conditional Niemann-Pick C mice demonstrate cell autonomous Purkinje cell neurodegeneration. *Hum Mol Genet* 2010;**19**(5):837-47. doi: 10.1093/hmg/ddp552.
33. Sarna JR, Larouche M, Marzban H, et al. Patterned Purkinje cell degeneration in mouse models of Niemann-Pick type C disease. *J Comp Neurol* 2003;**456**(3):279-91. doi: 10.1002/cne.10522.
34. Abi-Mosleh L, Infante RE, Radhakrishnan A, et al. Cyclodextrin overcomes deficient lysosome-to-endoplasmic reticulum transport of cholesterol in Niemann-Pick type C cells. *Proc Natl Acad Sci U S A* 2009;**106**(46):19316-21. doi: 10.1073/pnas.0910916106.
35. Liu B, Turley SD, Burns DK, et al. Reversal of defective lysosomal transport in NPC

disease ameliorates liver dysfunction and neurodegeneration in the npc1-/- mouse. *Proc Natl Acad Sci U S A* 2009;**106**(7):2377-82. doi: 10.1073/pnas.0810895106.

36. Orr HT Cell biology of spinocerebellar ataxia. *J Cell Biol* 2012;**197**(2):167-77. doi: 10.1083/jcb.201105092.

37. Pohl HBF, Porcheri C, Mueggler T, et al. Genetically Induced Adult Oligodendrocyte Cell Death Is Associated with Poor Myelin Clearance, Reduced Remyelination, and Axonal Damage. *Journal of Neuroscience* 2011;**31**(3):1069-1080. doi: 10.1523/Jneurosci.5035-10.2011.

38. Gallon M, Cullen PJ Retromer and sorting nexins in endosomal sorting. *Biochemical Society Transactions* 2015;**43**:33-47. doi: 10.1042/Bst20140290.

39. Hazan J, Fonknechten N, Mavel D, et al. Spastin, a new AAA protein, is altered in the most frequent form of autosomal dominant spastic paraplegia. *Nature Genetics* 1999;**23**(3):296-303. doi: Doi 10.1038/15472.

40. Solowska JM, Baas PW Hereditary spastic paraplegia SPG4: what is known and not known about the disease. *Brain* 2015;**138**(Pt 9):2471-84. doi: 10.1093/brain/awv178.

41. Lee H, Fenster RJ, Pineda SS, et al. Cell Type-Specific Transcriptomics Reveals that Mutant Huntingtin Leads to Mitochondrial RNA Release and Neuronal Innate Immune Activation. *Neuron* 2020;**107**(5):891-908 e8. doi: 10.1016/j.neuron.2020.06.021.

42. Ge P, Dawson VL, Dawson TM PINK1 and Parkin mitochondrial quality control: a source of regional vulnerability in Parkinson's disease. *Mol Neurodegener* 2020;**15**(1):20. doi: 10.1186/s13024-020-00367-7.

43. Wang W, Zhao F, Ma X, et al. Mitochondria dysfunction in the pathogenesis of

Alzheimer's disease: recent advances. *Mol Neurodegener* 2020;**15**(1):30. doi: 10.1186/s13024-020-00376-6.

44. Smith EF, Shaw PJ, De Vos KJ The role of mitochondria in amyotrophic lateral sclerosis. *Neurosci Lett* 2019;**710**:132933. doi: 10.1016/j.neulet.2017.06.052.

45. Stucki DM, Ruegsegger C, Steiner S, et al. Mitochondrial impairments contribute to Spinocerebellar ataxia type 1 progression and can be ameliorated by the mitochondria-targeted antioxidant MitoQ. *Free Radic Biol Med* 2016;**97**:427-440. doi: 10.1016/j.freeradbiomed.2016.07.005.

46. Ripolone M, Lucchini V, Ronchi D, et al. Purkinje cell COX deficiency and mtDNA depletion in an animal model of spinocerebellar ataxia type 1. *J Neurosci Res* 2018;**96**(9):1576-1585. doi: 10.1002/jnr.24263.

47. Ferro A, Carbone E, Zhang J, et al. Short-term succinic acid treatment mitigates cerebellar mitochondrial OXPHOS dysfunction, neurodegeneration and ataxia in a Purkinje-specific spinocerebellar ataxia type 1 (SCA1) mouse model. *PLoS One* 2017;**12**(12):e0188425. doi: 10.1371/journal.pone.0188425.

48. Chiang S, Huang MLH, Park KC, et al. Antioxidant defense mechanisms and its dysfunctional regulation in the mitochondrial disease, Friedreich's ataxia. *Free Radic Biol Med* 2020;**159**:177-188. doi: 10.1016/j.freeradbiomed.2020.07.019.

49. Liu L, Zhang K, Sandoval H, et al. Glial lipid droplets and ROS induced by mitochondrial defects promote neurodegeneration. *Cell* 2015;**160**(1-2):177-90. doi: 10.1016/j.cell.2014.12.019.

50. Davis R, Peters DH, McTavish D Valproic acid. A reappraisal of its pharmacological

properties and clinical efficacy in epilepsy. *Drugs* 1994;**47**(2):332-72.

51. Chateauvieux S, Morceau F, Dicato M, et al. Molecular and therapeutic potential and toxicity of valproic acid. *J Biomed Biotechnol* 2010;**2010**. doi: 10.1155/2010/479364.

ORIGINAL UNEDITED MANUSCRIPT

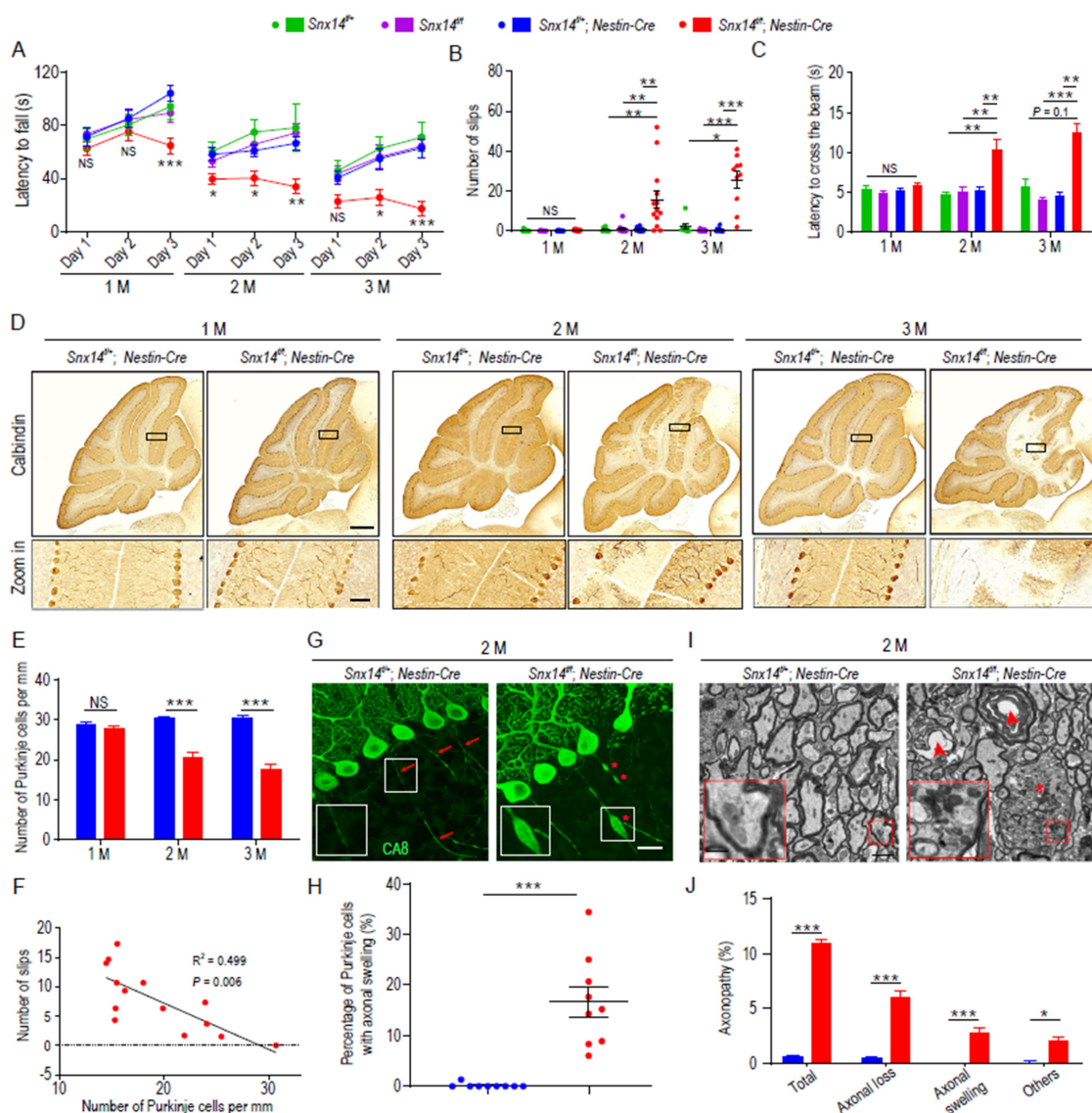


Figure 1. Progressive motor coordination deficits and Purkinje cell degeneration in *Snx14*-deficient mice. (A-C) Motor coordination in *Snx14*^{+/+}, *Snx14*^{ff/ff}, *Snx14*^{ff/+}; *Nestin-Cre* and *Snx14*^{ff/ff}; *Nestin-Cre* mice as determined by the rotarod and balance beam tests. (A) Quantification of the latency to fall in the rotarod test. *n* = 8~16 mice per genotype per age. The number of foot slips (B) and the latency to traverse the beam (C) in balance beam tests. *n* = 8~13 per genotype per age. (D) IHC labeling of calbindin⁺ Purkinje cells in *Snx14*^{ff/+}; *Nestin-Cre* and *Snx14*^{ff/ff}; *Nestin-Cre* mouse cerebella. Scale bars = 500 μm (top) and 50 μm (bottom). (E) Quantification of cerebellar Purkinje cells. *n* = 3 mice (total 8~9 slices). (F) The correlation between Purkinje cell density and the number of foot slips in balance beam tests. *n* = 14 *Snx14*^{ff/ff}; *Nestin-Cre* mice. (G) Immunofluorescence staining to detect CA8-positive Purkinje cells in the mouse cerebellum. Intact axons (arrows) and swollen axons (arrowheads). (H) Quantification of axonal swelling. (I) Electron microscopy images of CA8-positive cells. (J) Quantification of axonopathy.

ORIGINAL PAPER

(asterisks) are indicated. Scale bar = 20 μm . (H) The percentage of Purkinje cells with swollen axons in *Snx14^{fl/+};Nestin-Cre* mice ($n = 3$ mice, 1175 cells) and *Snx14^{fl/fl};Nestin-Cre* mice ($n = 3$ mice, 438 cells). (I) TEM analysis of Purkinje cell axons. The asterisk indicates a swollen axon, and arrowheads indicate axonal loss associated with a collapsed myelin sheath. Scale bar = 2 μm . (J) The percentage of Purkinje cells with axonopathies (axonal swelling, axonal loss and other types). $n = 3\sim 4$ mice. A total of 300~500 axons per mouse were scored. Male animals were used in (A-J). 1 M, 2 M, and 3 M represent 1 month, 2 months, and 3 months of age, respectively. All data represent means \pm S.E.M. P values were determined using repeated-measures ANOVA with Bonferroni's *post hoc* analysis in (A), the Kruskal-Wallis test with Dunn's *post hoc* analysis in (B) and (C), Student's t test in (E), (H) and (J) and Spearman's rank correlation in (F). NS, not significant; * $P < 0.05$; ** $P < 0.01$; *** $P < 0.001$.

ORIGINAL UNEDITED MANUSCRIPT

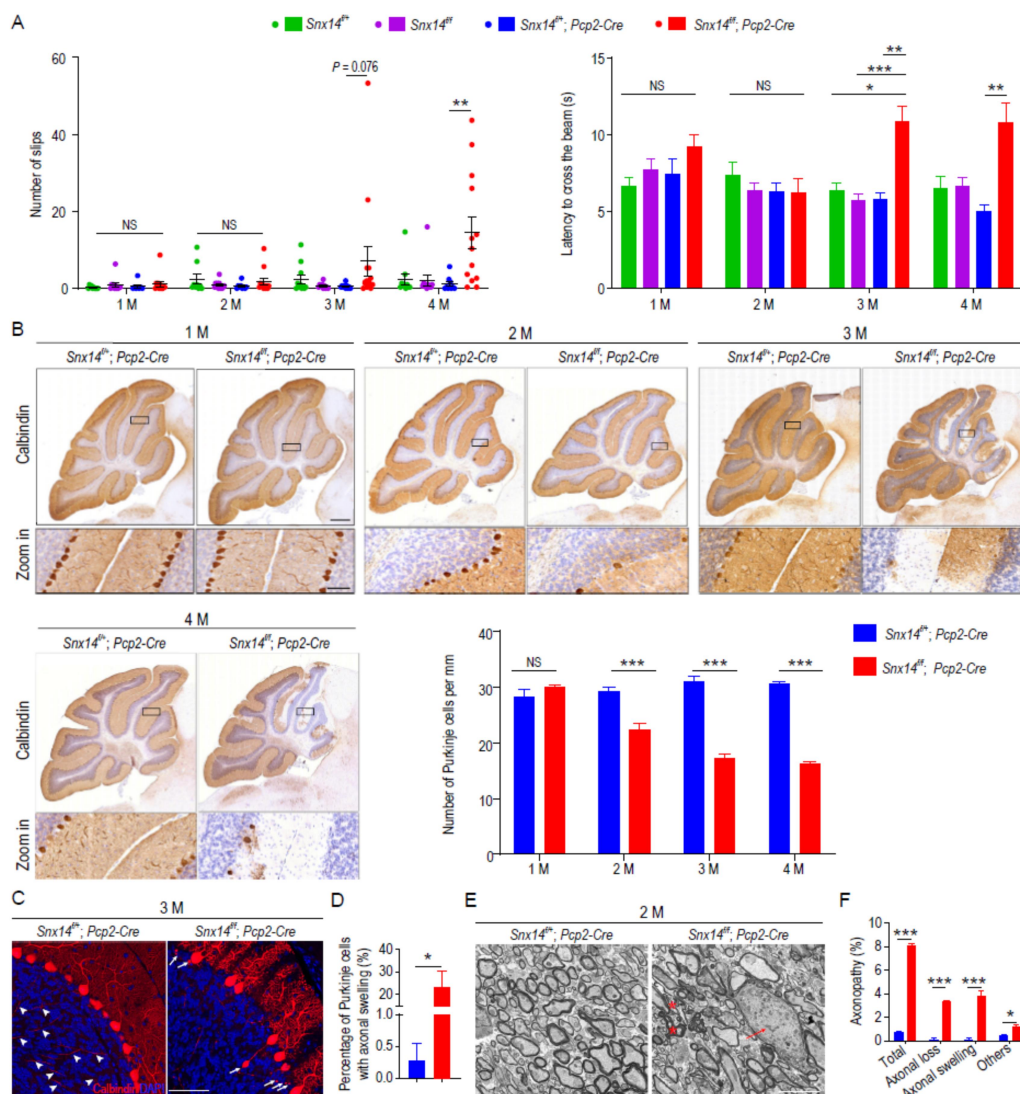


Figure 2. SNX14 deficiency induces cell-autonomous degeneration of Purkinje cells. (A) Quantification of foot slips (top) and the latency to traverse the beam (bottom) in balance beam tests in male mice ($n = 8\sim 14$ mice). (B) IHC labeling and quantification of calbindin⁺ Purkinje cells in the cerebella of female *Snx14^{+/+};Pcp2-Cre* and *Snx14^{ff};Pcp2-Cre* mice. Scale bars = 500 μm (top) and 50 μm (bottom), $n = 3$ mice. (C) Immunofluorescence staining of calbindin⁺ Purkinje cells in female *Snx14^{+/+};Pcp2-Cre* and *Snx14^{ff};Pcp2-Cre* mouse cerebella. Arrowheads (left) indicate intact axons, and arrows (right) indicate swollen axons. Scale bar = 50 μm . (D) The percentage of Purkinje cells with swollen axons in *Snx14^{+/+};Pcp2-Cre* mice ($n = 3$ mice, 399 cells) and *Snx14^{ff};Pcp2-Cre* mice ($n = 3$ mice, 174 Purkinje cells). (E) Representative TEM images of transverse cerebellar tissue sections. The arrow indicates a swollen axon, and asterisks indicate axonal loss with a collapsed myelin sheath. Scale bar = 5 μm . (F) The percentage of Purkinje cells with axonopathies (axonal loss, axonal swelling and other types). $n = 3\sim 4$ mice per genotype; 300~500

ACCEPTED MANUSCRIPT

ORIGINAL MANUSCRIPT

axons per mouse were scored. 1 M, 2 M, 3 M, and 4 M indicate 1~4 months of age. All data represent means \pm S.E.M. *P* values were determined using the Kruskal-Wallis test with Dunn's *post hoc* analysis in (A) and Student's *t* test in (B), (D) and (F). NS, not significant; **P* < 0.05; ***P* < 0.01; ****P* < 0.001.

ORIGINAL UNEDITED MANUSCRIPT

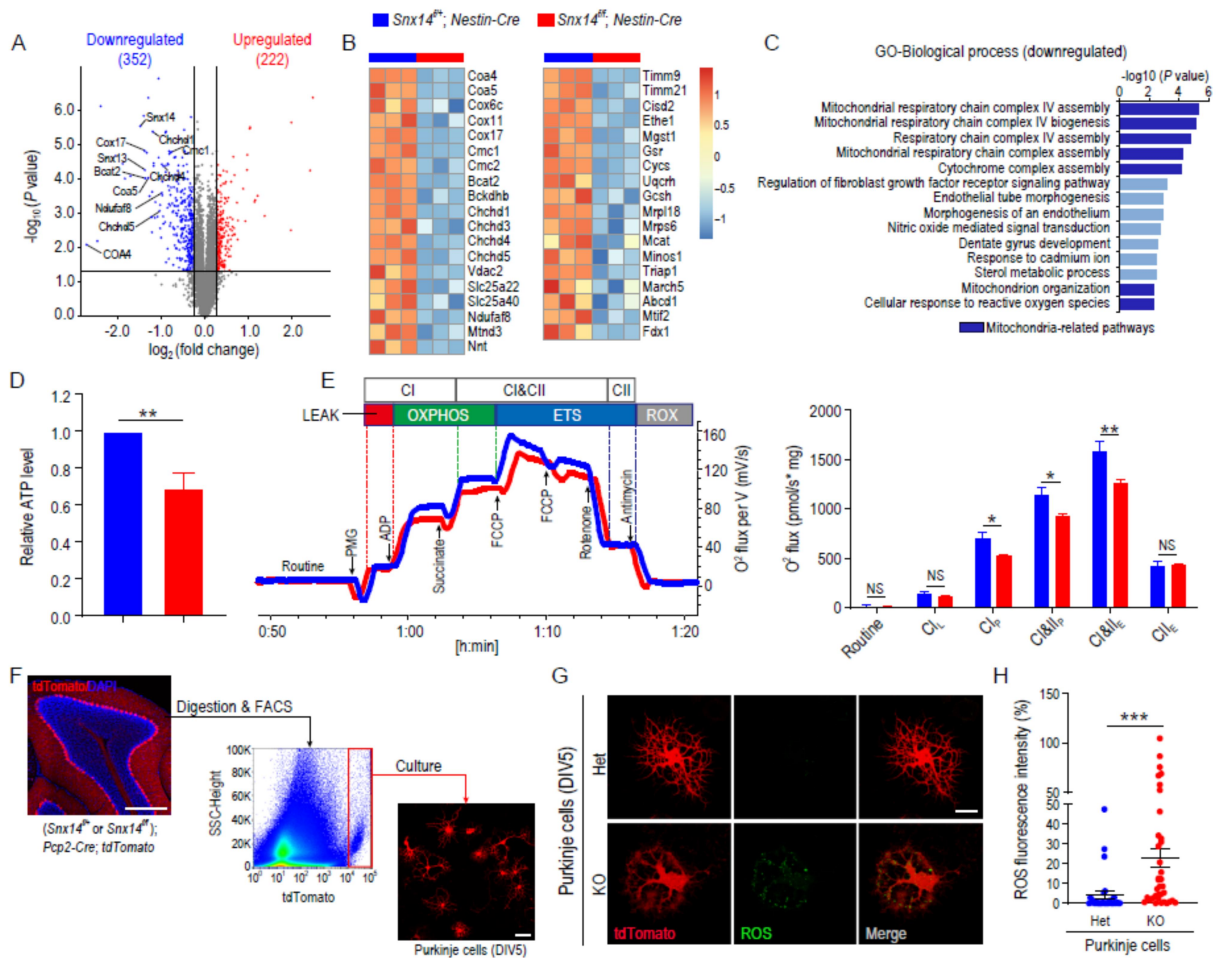


Figure 3. Mitochondrial dysfunction in the *Snx14*-deficient mouse cerebellum.

(A) Proteomic analysis of the mouse cerebellum: volcano plot illustrating upregulated (red) and downregulated (blue) proteins in 1-month-old *Snx14^{fl/fl};Nestin-Cre* compared to *Snx14^{fl/+};Nestin-Cre* mouse cerebella (fold change > 1.2, *P* value < 0.05). *n* = 3 samples. Each sample was derived from cerebellar tissue pooled from 3 mice of the same genotype. (B) Heatmap depicting downregulated mitochondrial proteins in the *Snx14^{fl/fl};Nestin-Cre* mouse cerebellum. (C) GO analysis of downregulated proteins in the *Snx14^{fl/fl};Nestin-Cre* mouse cerebellum. Mitochondria-related pathways are marked in dark blue. (D) Quantification of ATP levels in 1-month-old *Snx14^{fl/+};Nestin-Cre* and *Snx14^{fl/fl};Nestin-Cre* mouse cerebella. (E) Representative respirometric traces from cerebellar homogenates in 1.5-month-old *Snx14^{fl/+};Nestin-Cre* (*n* = 10 mice) and *Snx14^{fl/fl};Nestin-Cre* mice (*n* = 15 mice) using high-resolution FluoRespirometry. (F) Experimental outline, FACS isolation and *in vitro* culture of tdTomato⁺ Purkinje cells from P6 *Snx14^{fl/+};Pcp2-Cre;tdTomato* and *Snx14^{fl/fl};Pcp2-Cre;tdTomato* cerebella. Scale bars = 500 μm (left) and 50 μm (right). (G) Visualization of ROS production in *Snx14* Het and KO Purkinje cells (DIV5) using DCFH-DA (green). Scale bar = 20 μm. (H) Quantification of ROS fluorescence intensity in Het (*n* = 28 cells) and KO (*n* = 38 cells) Purkinje cells. Male animals were

used in (A-E). All data represent means \pm S.E.M. *P* values were determined using the Student's *t* test in (D), (E) and (H). NS, not significant; **P* < 0.05; ***P* < 0.01; ****P* < 0.001.

ORIGINAL UNEDITED MANUSCRIPT

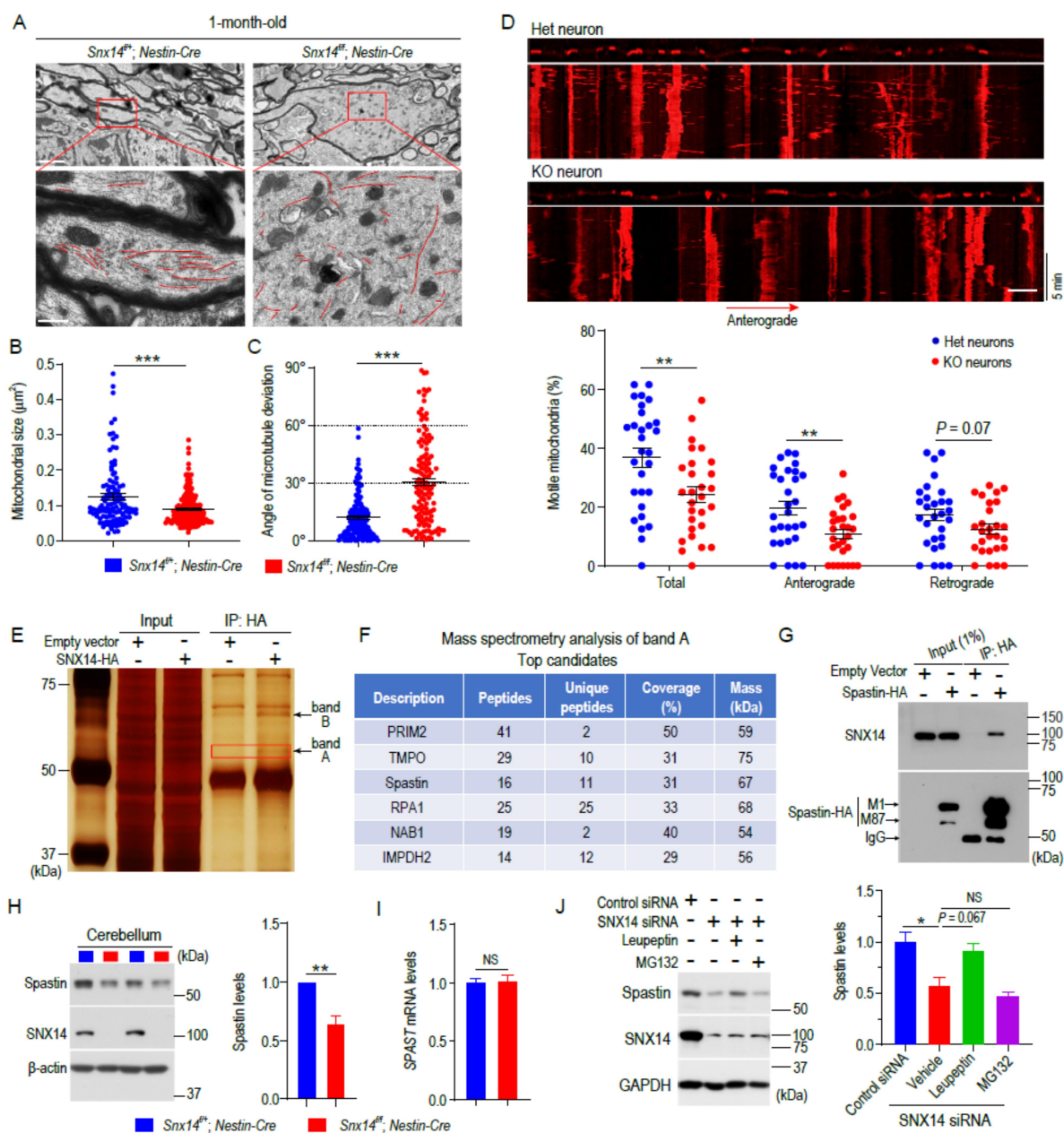


Figure 4. SNX14 deficiency disrupts microtubule organization and mitochondrial transport in axons. (A) TEM analysis of longitudinal sections from Purkinje cell axons in male *Snx14^{fl/+};**Nestin-Cre* and *Snx14^{fl/fl};**Nestin-Cre* mice. Microtubules are traced with red lines (bottom). Scale bars = 2 μm (top) and 0.5 μm (bottom). (B) Quantification of mitochondrial size and (C) orientation (angle of microtubule deviation) in swollen axons from Purkinje cells. Each plot represents a single microtubule filament or mitochondrion (at least 9 TEM images per genotype were analyzed and pooled for statistical analysis). $n = 3\sim 5$ mice per genotype. (D) Representative kymographs and quantitative analysis of mitochondrial transport in axons from *Snx14^{fl/+};**Nestin-Cre* (Het) and *Snx14^{fl/fl};**Nestin-Cre* (KO) neurons. Scale

ORIGINAL PAPER

bar = 5 μ m. $n = 28\sim 29$ cells in each group. (E) Two specific bands (bands A and B, indicated by arrows) were identified in HA-immunoprecipitates from HEK293T cell lysates transfected with SNX14-HA (silver stain). (F) Six SNX14-interacting proteins were identified using mass spectrometry analysis from the excised band A in (E) (red box). (G) Co-IP between exogenously expressed spastin-HA (isoforms M1 and M87) and endogenous SNX14 protein. IP, immunoprecipitation. (H) Immunoblot analysis of spastin in cerebella from 1-month-old mice. Signal intensities from immunoblots were normalized to β -actin. $n = 5$. (I) *SPAST* mRNA levels quantified using qRT-PCR in the cerebellum of 1-month-old mice. $n = 6$ mice. (J) Immunoblot analysis of spastin in cell lysates from SNX14-depleted HEK293T cells treated with a lysosomal inhibitor (leupeptin) or proteasomal inhibitor (MG132). $n = 3$. All data represent means \pm S.E.M. *P* values were determined using Student's *t* test in (B), (C), (D), (H) and (I) and one-way ANOVA with Tukey's *post hoc* analysis in (J). NS, not significant; **P* < 0.05; ***P* < 0.01; ****P* < 0.001.

ORIGINAL UNEDITED MANUSCRIPT

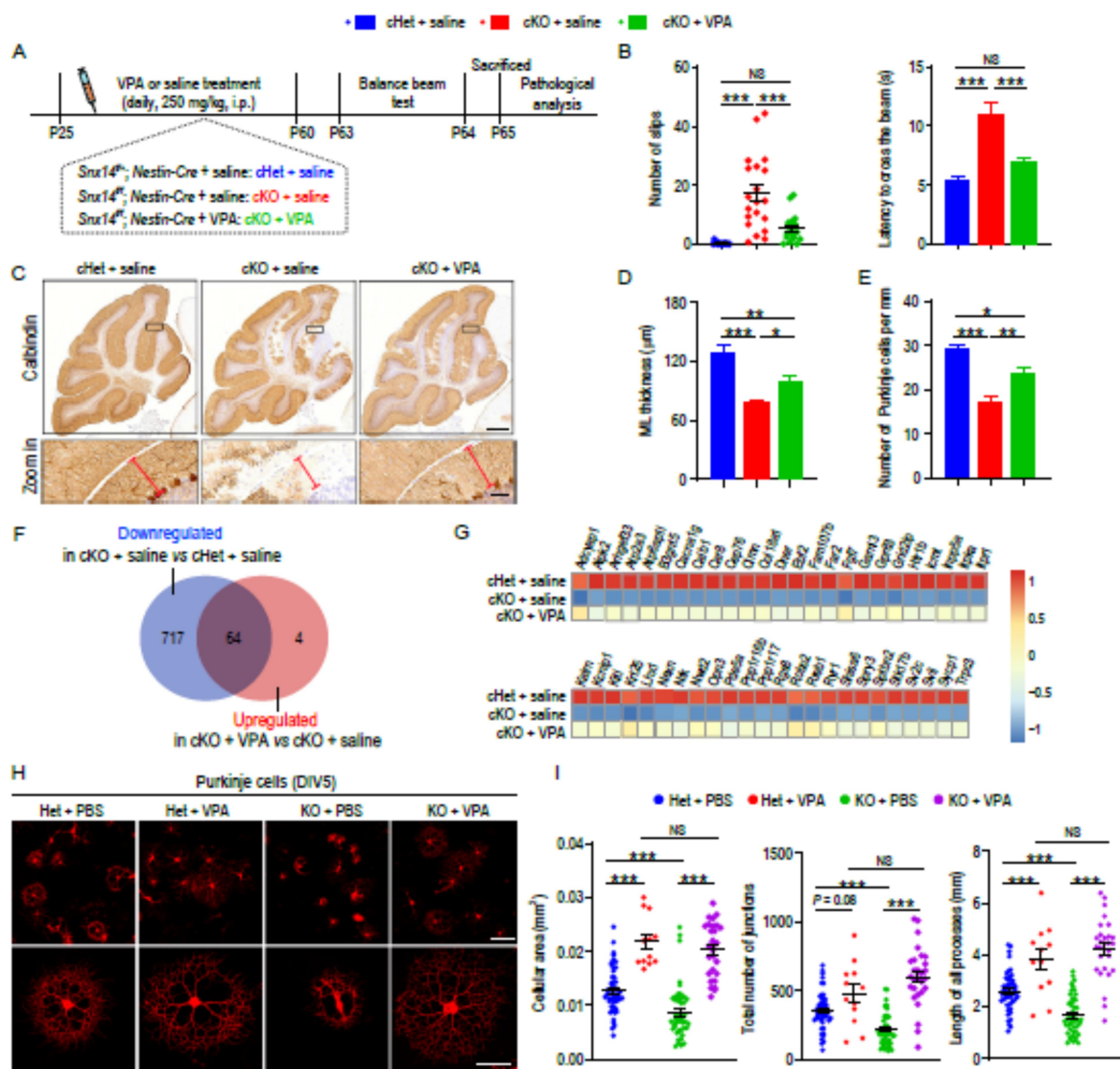


Figure 5. VPA treatment ameliorates cerebellar ataxia and Purkinje cell death in *Snx14*-deficient mice. (A) Schematic timeline of VPA rescue experiments. The three treatment groups in the study include: *Snx14*^{+/+}; *Nestin-Cre* + saline (cHet + saline), *Snx14*^{fl/fl}; *Nestin-Cre* + saline (cKO + saline) and *Snx14*^{fl/fl}; *Nestin-Cre* + VPA (cKO + VPA). Mice (P25) were intraperitoneally (i.p.) injected with saline or VPA (250 mg/kg/day) for 5 weeks, followed by behavioral and pathological analyses. (B) Quantification of mouse foot slips (left) and the latency to traverse the beam (right) in balance beam tests. *n* = 15~20 mice. (C) Representative images of calbindin-expressing Purkinje cells in cHet + saline, cKO + saline and cKO + VPA mice. Scale bars = 500 μ m (top) and 50 μ m (bottom). (D) Measurement of cerebellar ML thickness upon VPA treatment. *n* = 3~4 mice. (E) Histological analyses to determine the effects of VPA on Purkinje cell survival. *n* = 3~5 mice. (F and G) Transcriptomic analysis of 2-month-old male cHet + saline, cKO + saline and cKO + VPA mice (fold change > 1.2; adjusted *P* value < 0.1). *n* = 7 mice per group. (F) Venn

ORIGINAL PAPER

diagram depicting downregulated genes in the cKO + saline group compared to the cHet + saline group (blue circle) and upregulated genes in the cKO + VPA group relative to the cKO + saline group (red circle); 64 genes in the overlap region indicate downregulated genes with SNX14 deletion restored by VPA treatment. (G) Heatmap depicting Purkinje cell-specific genes within the 64 genes showing VPA-dependent normalization. (H) Representative images of Het and KO Purkinje cells upon saline or VPA treatment. Scale bars = 100 μm (top) and 50 μm (bottom). (I) Quantification of the cellular area (left), total number of junctions (center) and the summed length of all processes (right) in Purkinje cells in the Het + PBS ($n = 56$ cells), Het + VPA ($n = 12$ cells), cKO + PBS ($n = 46$ cells) and cKO + VPA ($n = 28$ cells) groups. Male animals were used in (A-I). All data represent means \pm S.E.M. P values were determined using one-way ANOVA with Tukey's *post hoc* analysis. NS, not significant; * $P < 0.05$; ** $P < 0.01$; *** $P < 0.001$.

ORIGINAL UNEDITED MANUSCRIPT

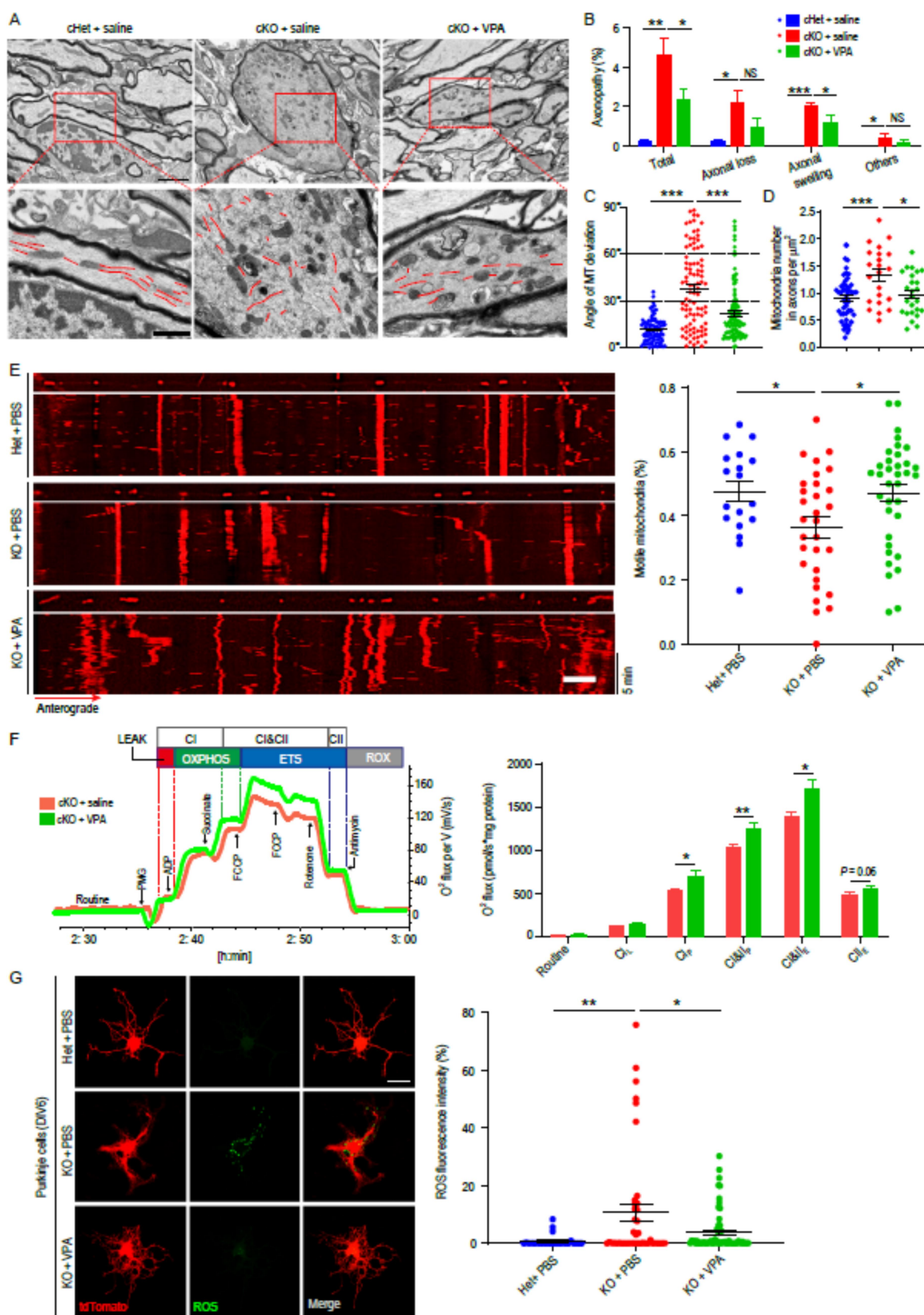


Figure 6. VPA promotes Purkinje cell survival by restoring mitochondrial function. (A) Representative TEM images of longitudinal sections of Purkinje cell

axons from cHet + saline, cKO + saline and cKO + VPA mice. Microtubules are traced with red lines (bottom). Scale bars = 2 μm (top) and 1 μm (bottom). (B) Quantification of axonopathies (axonal loss, axonal swelling and other types) of Purkinje cells. $n = 3\sim 4$ mice. A total of 300~500 axons per mouse were scored. (C) Quantification of orientation (angle of microtubule deviation) in swollen axons from Purkinje cells. Each plot represents a single microtubule filament (at least 10 TEM images per genotype were analyzed and pooled for statistical analyses). $n = 3\sim 5$ mice per genotype. (D) Quantification of mitochondria in Purkinje cell axons. $n = 4$ mice. A total of 20~50 axons per group were scored. (E) Representative kymographs and quantification of motile mitochondria in the axons of Het + PBS ($n = 18$ cells), KO + PBS ($n = 30$ cells), and KO + VPA ($n = 35$ cells) neurons. Scale bar = 5 μm . (F) Characterization of mitochondrial function in cKO + saline ($n = 11$ mice) and cKO + VPA ($n = 11$ mice) mouse cerebella using high-resolution FluoRespirometry. (G) Visualization and quantification of ROS production in Het + saline ($n = 26$ cells), KO + saline ($n = 42$ cells) and KO + VPA ($n = 59$ cells) Purkinje cells using DCFH-DA (green). Scale bar = 25 μm . All data represent means \pm S.E.M. P values were determined using one-way ANOVA with Tukey's *post hoc* analysis in (B), (C), (D), (E), (G) and Student's *t* test in (F). NS, not significant; * $P < 0.05$; ** $P < 0.01$; *** $P < 0.001$.

ORIGINAL UNEDITED MANUSCRIPT